



저작자표시-비영리-변경금지 2.0 대한민국

이용자는 아래의 조건을 따르는 경우에 한하여 자유롭게

- 이 저작물을 복제, 배포, 전송, 전시, 공연 및 방송할 수 있습니다.

다음과 같은 조건을 따라야 합니다:



저작자표시. 귀하는 원저작자를 표시하여야 합니다.



비영리. 귀하는 이 저작물을 영리 목적으로 이용할 수 없습니다.



변경금지. 귀하는 이 저작물을 개작, 변형 또는 가공할 수 없습니다.

- 귀하는, 이 저작물의 재이용이나 배포의 경우, 이 저작물에 적용된 이용허락조건을 명확하게 나타내어야 합니다.
- 저작권자로부터 별도의 허가를 받으면 이러한 조건들은 적용되지 않습니다.

저작권법에 따른 이용자의 권리는 위의 내용에 의하여 영향을 받지 않습니다.

이것은 [이용허락규약\(Legal Code\)](#)을 이해하기 쉽게 요약한 것입니다.

[Disclaimer](#)

이학석사 학위논문

East Asian atmospheric rivers
modulated by Pacific–Japan
pattern

Pacific–Japan 패턴에 의한
동아시아 atmospheric river의 조절

2023년 8월

서울대학교 대학원

지구환경과학부

권 예 은

East Asian atmospheric rivers
modulated by Pacific–Japan
pattern

지도교수 손 석 우

이 논문을 이학석사 학위논문으로 제출함
2023년 5월

서울대학교 대학원
지구환경과학부
권 예 은

권예은의 이학석사 학위논문을 인준함
2023년 7월

위 원 장 _____ 김 정 훈 _____ (인)

부위원장 _____ 손 석 우 _____ (인)

위 원 _____ 김 진 원 _____ (인)

Abstract

Atmospheric rivers (ARs), which are filamentary objects of intense water vapor transport, play a critical role in shaping the hydroclimate of East Asia. While recent studies have improved our understanding of the climatological features of East Asian ARs, their temporal variability is still not well understood. This study examines the subseasonal variability of East Asian ARs that is associated with the Pacific–Japan (PJ) teleconnection pattern during boreal summer. The East Asian ARs are strongly modulated by the PJ pattern. During the positive PJ, the Western North Pacific subtropical high expands northwestward, and this results in pronounced AR activities over Korea and Japan. When the negative PJ develops, the subtropical high retreats southward but extends westward, resulting in enhanced AR impacts over eastern China. The duration of AR events also increases in the AR–favorable PJ phases, i.e., positive PJ in Korea–Japan and negative PJ in eastern China, implying higher risks of hazardous AR impacts in the respective regions. These changes are closely related to the PJ–related quasi–stationary moisture transport with a relatively minor contribution of transient weather systems. This result suggests that East Asian ARs can be better understood and predicted by monitoring the PJ pattern.

Keyword: atmospheric river, Pacific–Japan pattern, subseasonal variability

Student Number: 2021–26855

Table of Contents

List of figures	i
1. Introduction	1
2. Data and Methods	5
2.1 Dataset	5
2.2 PJ index.....	6
2.3 Multiscale index of ARs	8
3. Results	9
3.1 AR responses to PJ pattern	9
3.2 Modulation of hazardous versus beneficial AR events.....	12
3.3 Multiscale diagnosis of PJ modulation of ARs	15
3.4 Related weather systems.....	17
4. Summary and discussion	21
References.....	25
Figures.....	36
Abstract in Korean	49

List of figures

Figure 1. The normalized time series distribution of the PJ index during positive PJ (red line), and negative PJ (blue line). The thin lines indicate individual PJ event indices, while the thick lines are the average. The black lines denote the ± 1 standard deviation of the PJ index.

Figure 2. The number of positive PJ events (red bars), and negative PJ events (blue bars) in June, July, and August from 1979 to 2020.

Figure 3. (a) JJA climatology of **IVT** ($> 150 \text{ kg m}^{-1} \text{ s}^{-1}$, vectors), and 850-hPa GPH (gpm, contoured). (b), (c) As in (a) but for (b) positive PJ, and (c) negative PJ. (d) JJA climatology of AR frequency (%), shaded), and 850-hPa (gpm, contoured). (e), (f) Differences of AR frequency (%), shaded), and 850-hPa GPH (gpm, contoured) from JJA climatologies for (e) positive PJ, and (f) negative PJ. Only the statistically significant differences are shown based on two-tailed student's t test at the 95% confidence level. The number of degrees of freedom corresponds to the number of PJ events. In (a)–(f), the WNPSH boundary is highlighted by a bold 1,480-gpm contour. The black boxed regions in (e), (f) denote the Korea–Japan ($35\text{--}45^\circ \text{ N}$, $124\text{--}144^\circ \text{ E}$) and eastern China ($25\text{--}35^\circ \text{ N}$, $106\text{--}122^\circ \text{ E}$) domains in this study.

Figure 4. As in Fig. 3d–f, but derived from the original Guan and Waliser (2015) algorithms.

Figure 5. (a) JJA climatology of AR precipitation (mm day^{-1} , shaded). (b), (c) Differences in AR precipitation (mm day^{-1} , shaded) from JJA climatologies for (b) positive PJ, and (c) negative PJ. Only the statistically significant difference is displayed based on two-tailed student's t test at the 95% confidence level. The number of degrees of freedom corresponds to the number of independent PJ events. (d)–(f) As in (a)–(c), but for AR precipitation ratio (%), shaded)

Figure 6. (a),(b) Fraction of AR events for five different AR scales (see the right diagram) during positive PJ (red line), and negative PJ (blue line) in (a) Korea–Japan, and (b) eastern China. Filled circles indicate statistically significant differences between the two PJ phases based on two-tailed student’ s t test at the 95% confidence level. Red and blue bars represent the difference in fraction (%) from JJA climatology for positive PJ, and negative PJ, respectively. Hatched bars indicate statistically significant differences between the JJA and each PJ phase based on two-tailed student’ s t test at the 95% confidence level. (c),(d) Differences in maximum IVT (left y-axis), and AR duration (right y-axis) for AR events from JJA climatologies in the (c) Korea–Japan, and (d) eastern China for positive PJ (red box), and negative PJ (blue box). The ARs whose centroids are located in the boxed regions in Figs. 3e,f are considered.

Figure 7. The number of AR events during 1979–2020 JJA depending on AR scales (shaded) overlaid with 850–hPa GPH climatology (gpm, contoured). The WNPSH boundary is highlighted by a bold 1,480–gpm contour.

Figure 8. JJA climatology of (a) AR–related $IVTA_{HF}$ ($\text{kg m}^{-1} \text{s}^{-1}$, shaded), and (b) AR–related $IVTA_{LF}$ ($\text{kg m}^{-1} \text{s}^{-1}$, shaded) overlaid with 850–hPa GPH (gpm, contoured). The AR–related IVTA components are determined by considering the spatial overlap of AR and IVTA.

Figure 9. (a),(b) PDF (%) of ARs in (a) Korea–Japan, and (b) eastern China as a function of MI during JJA (black line), positive PJ (red bars), and negative PJ (blue bars). (c),(d) Differences in $IVTA_{HF}^{AR}$ (left y-axis), $IVTA_{LF}^{AR}$ (left y-axis), and MI (right y-axis) from JJA climatologies in the (c) Korea–Japan, and (d) eastern China for positive PJ (red box), and negative PJ (blue box). The ARs whose centroids are located in the boxed regions in Figs. 3e,f are considered.

Figure 10. (a)–(f) AR–relative composites of (top) 850–hPa GPHA (gpm, contoured) and IVTA ($\text{kg m}^{-1} \text{s}^{-1}$, shaded), and their (middle)

HF and (lower) LF components during (a)–(c) JJA, (d)–(f) positive PJ for ARs in Korea–Japan. Only the statistically significant GPHA is shown based on two-tailed student's *t* test at the 95% confidence level. Stipples indicate the statistically significant IVTA. The number of degrees of freedom is determined by regarding consecutive six-hourly AR snapshots as one event. (g)–(i) As in (a)–(c), but for ARs in eastern China. (j)–(l) As in (d)–(f), but for ARs in eastern China during negative PJ. In (f),(l), “A” and “C” indicate the PJ-related LF anticyclone and cyclone, respectively. The ARs whose centroids are located in the boxed regions in Figs. 3e,f are considered.

Figure 11. As in Fig. 10, but for (a)–(c) ARs in Korea–Japan during negative PJ, and (d)–(f) ARs in eastern China during positive PJ.

1. Introduction

Atmospheric rivers (ARs) are filamentary objects of intense water vapor transport and play a substantial role in shaping the global and regional hydroclimate. Early AR studies have focused on the cool-season ARs affecting western coasts of North America (Bao et al., 2006; Ralph et al., 2006; Neiman et al., 2008; Dettinger et al., 2011; Ralph & Dettinger, 2012). However, ARs are now considered ubiquitous across the regions including monsoon regions (Dhana Laskhmi & Satyanarayana, 2020; Liang & Yong, 2021; Park et al. 2021), Southern Hemisphere (Viale et al., 2018; Ye et al., 2020), and even in high latitudes (Nash et al., 2018; Wille et al., 2019) and continental interiors (Nayak & Villarini, 2017; Akbary et al., 2019). As such, ARs play a critical role in both regional and global hydroclimate (Waliser & Guan, 2017; Paltan et al., 2017), although their formation mechanisms could be spatioseasonally different (Gimeno et al. 2021; Park et al. 2023).

Among others, East Asia is increasingly noticed as one of the region most susceptible to AR impacts. East Asian ARs are

observed throughout the year (Kamae et al., 2017a,b), but they are most pronounced in the summer monsoon period (Mundhenk et al., 2016; Pan & Lu, 2020; Liang & Yong, 2021). The summer prevalence of East Asian ARs is related to the western North Pacific subtropical high (WNPSH) which expands close to the Asian continent and thereby facilitates AR formation through enhanced monsoon southwesterly (Pan & Lu 2020; Park et al., 2021). About 35–70% of summer monsoon rainfall is associated with ARs (Park et al. 2021; Kim et al. 2021; Kwon et al., 2022). The East Asian ARs are particularly active in early monsoon period (June–July) when the WNPSH extends westward with enhanced pressure gradient along its northern boundary (Park et al. 2021). Although reduced in late monsoon period (August–September), ARs are still observed along the northern flank of the WNPSH.

In addition to distinct seasonal and subseasonal climatologies, East Asian ARs are also characterized by significant interannual variability. Kamae et al. (2017a) found that East Asian ARs become enhanced in the post-El Niño summer. The anomalous warm Indian Ocean in the El Niño-

decaying season drives the Kelvin wave-induced Ekman divergence over the subtropical western North Pacific, leading to the anomalous westward extension of the WNPSH, a process known as Indo-western Pacific Ocean capacitor effect (Xie et al., 2009, 2016). This reinforces the low-level monsoon southwesterly with increased AR occurrences in East Asia (Kamae et al., 2017a,b; Naoi et al., 2020).

The aforementioned studies indicate that the climatology and variability of East Asian summer ARs are closely associated with the WNPSH. However, there is a lack of investigation into how the ARs are modulated by the Pacific-Japan (PJ) teleconnection pattern. The PJ pattern is typically characterized by meridionally propagating low-level Rossby wave train forced by convective activity around the Philippine Sea (Nitta, 1987; Kosaka & Nakamura 2006). The enhanced tropical convection excites the positive PJ pattern featured by the northward expansion of the WNPSH (Figure 3b), while the suppressed convection excites the negative PJ pattern with meridionally-confined but westward-extended WNPSH (Figure 3c). The WNPSH variability associated with the PJ pattern brings the

anomalously wet and dry periods in East Asia (Kosaka et al., 2011; Kubota et al., 2016; Noh et al., 2021). Although not documented in the literature, the PJ modulation of East Asian hydroclimate is conjectured to be to some extent via the modulation of AR activity given the fact that the AR activity is greatly synchronized with the WNPSH variability.

The present study first documents the close relationship between East Asian AR variability and the PJ pattern. This is achieved by utilizing the long-term AR catalog and PJ index (Section 2). The AR frequency and its rainfall impacts are compared between the positive and negative PJ patterns (Section 3.1). The hydrological impacts of ARs in the two phases are further detailed by considering the hazardous and beneficial AR events (Section 3.2). The key process behind the PJ modulation of East Asian ARs is analyzed by using a recently-devised multiscale AR index (Section 3.3). In the last, the results are summarized along with a discussion (Section 4).

2. Data and Methods

2.1. Dataset

The fifth-generation European Centre for Medium-range Weather Forecasts atmospheric reanalysis (ERA5; Hersbach et al., 2020) data is used. All variables are used in 37 pressure levels with a horizontal resolution of $1.5^\circ \times 1.5^\circ$ and a temporal resolution of 6 h for 1979–2020. The anomaly is defined as the deviation from the daily climatology. For the precipitation analysis, the gauge-based daily precipitation analysis from the Climate Prediction Center (CPC; Xie et al., 2007) dataset with a resolution of $0.5^\circ \times 0.5^\circ$ is used. As the influence of the PJ pattern is dominant in the summer, only June–August (JJA) is considered.

For AR analyses, we use the 42-year AR catalog produced by Park et al. (2023) who applied the modified AR detection algorithm of Guan and Waliser (2015) to ERA5 data with same spatiotemporal resolution. The algorithm

automatically detects ARs based on integrated water vapor transport (IVT) anomaly (IVTA) where IVT is computed as

$$\mathbf{IVT} = |\mathbf{IVT}|, \mathbf{IVT} = -\frac{1}{g} \int_{1000 \text{ hPa}}^{300 \text{ hPa}} q(\mathbf{u}\mathbf{i} + \mathbf{v}\mathbf{j})dp \quad (1)$$

where \mathbf{i} and \mathbf{j} are the unit vectors in the zonal and meridional directions, respectively; u and v are the zonal and meridional winds, respectively; q is the specific humidity; g is the gravitational acceleration. The algorithm first searches for an object as a collection of grid points with $\text{IVTA} > 150 \text{ kg m}^{-1} \text{ s}^{-1}$. The geographical conditions (length $> 2000 \text{ km}$ and length-to-width ratio > 2) are applied to filter out a non-filamentary object. An object trapped in the deep tropics without a considerable poleward moisture transport is also discarded by examining the location of AR centroid and the object-mean \mathbf{IVT} . Readers are referred to Park et al. (2023) for details.

2.2. PJ index

The PJ pattern is identified by computing a point-based PJ index suggested by Kubota et al. (2016). The index is defined as the difference of the normalized 850-hPa

geopotential height (GPH) anomaly (GPHA) between Taiwan (22 °N, 120 °E) and Japan (35 °N, 140 °E) as

$$\text{PJ index} = [\text{GPHA}^*_{35^\circ\text{N},140^\circ\text{E}} - \text{GPHA}^*_{22^\circ\text{N},120^\circ\text{E}}] / 2 \quad (2)$$

where asterisk indicates the normalization by the standard deviation of the values for each grid point. To eliminate the transient fluctuation, a 10-day Lanczos low pass filter is applied to the index (Duchon, 1979). The positive and negative PJ events are selected based on ± 1.0 standard deviation of the PJ index. In order to ensure the independence of the samples, the individual PJ events (either positive or negative) are separated by at least one day. The positive PJ events are characterized by southwest–northeast dipole of anomalous cyclone over the Philippine Sea and anomalous anticyclone over Japan (Figure 3e). The negative PJ patterns exhibit the mirrored anticyclone–cyclone dipole (Figure 3f). On average, both of the positive and negative PJ patterns last 5 days (Figure 1). The specific PJ events are not concentrated in a particular month, but are evenly distributed throughout the season

(Figure 2). Consequently, the subsequent analyses are not significantly affected by the monthly variation of PJ events.

2.3. Multiscale index of ARs

The underlying mechanism for AR modulation by PJ patterns is investigated by using a AR multiscale index (MI; Park et al. 2023):

$$MI = \frac{IVTA_{HF}^{AR}}{IVTA^{AR}} \quad (3)$$

Here, $IVTA^{AR} = IVTA_{HF}^{AR} + IVTA_{LF}^{AR}$, and $IVTA_{HF}^{AR}$ and $IVTA_{LF}^{AR}$ are the AR-mean high- (HF) and low-frequency (LF) IVTA, respectively. The Lanczos filter is applied with a 10-day period cutoff. The MI measures the relative importance of HF and LF IVTA to ARs. The MI is set to 0 for negative $IVTA_{HF}^{AR}$ (i.e., $IVTA^{AR} < IVTA_{LF}^{AR}$) and 1 for negative $IVTA_{LF}^{AR}$ (i.e., $IVTA^{AR} < IVTA_{HF}^{AR}$) so that MI ranges from 0 to 1. The closer MI is to 1, an AR is dominated by transient moisture transport, while an AR with MI closer to 0 is more closely associated with quasi-stationary moisture transport.

3. Results

3.1. AR responses to PJ pattern

The WNPSH and AR frequency during the positive and negative PJ are compared with their JJA climatologies (Figure 3). The AR frequency is defined as the percentage ratio of the number of AR-existing time steps to the number of all time steps at each grid point. The climatological southwesterly **IVT** organizes along the boundary of the WNPSH (Figure 3a; see bold contour for the WNPSH boundary). The AR activity is pronounced in the same region with a maximum frequency of $\sim 20\%$ in the baiu frontal zone and the Pacific open ocean (Figure 3d). The spatial coherence of monsoon southwesterly and AR activity has been well documented in the literature (Pan & Lu, 2020; Park et al., 2021).

However, both the WNPSH and AR frequency substantially change when the PJ pattern develop (Figures 3b,e and 3c,f). When the positive PJ develops, the northern boundary of the WNPSH shifts northward with a well-defined

ridge around the Korean Peninsula and monsoon trough over the Philippine Sea (Figure 3b). This directly results from the positive PJ anomalies—cyclone–anticyclone dipole in the southwest–northeast direction (Figure 3e). The AR activity is enhanced over Korea–Japan and the Philippine Sea but suppressed in southeastern China and the Pacific open ocean. When negative PJ develops, on the contrary, the WNPSH retreats southward but extends westward (Figure 3c) due to the anticyclone–cyclone dipole (Figure 3f). The AR activity also exhibits a mirrored change from that in the positive PJ. The PJ modulation of AR activity is robustly found when the original version of Guan and Waliser (2015) algorithm is used in AR detection (Figure 4).

Figure 5 compares the AR precipitation and its ratio to total precipitation between JJA, positive PJ and negative PJ. Here, AR precipitation is defined as precipitation in a grid where AR is identified for at least 12 hours per day (i.e., two time steps; not necessarily consecutive). To consider the spatial coincidence, the AR grids are linearly interpolated into the CPC grids. In the climatological sense, AR precipitation is

widely distributed along the Meiyu–Changma–Baiu region (Figure 5a) with a local maximum ($\sim 8 \text{ mm day}^{-1}$) in western Japan. The ARs accounts for 30–50% of summer rainfall in eastern China, and over 60% in Korea and western Japan (Figure 5d), consistent with previous quantification (Park et al., 2021).

During the positive PJ, AR precipitation increases in Korea (by up to 3 mm day^{-1}) but decreases in inland eastern China (by $1\text{--}2 \text{ mm day}^{-1}$; Figure 5b). The increase is also marginally observed in the southeast coast of China. The mirrored AR precipitation change is evident during the negative PJ (Figure 5c). This is consistent with the AR frequency change in Figures 3e,f. However, the AR precipitation change is not simply proportional to total precipitation change. When analyzing the difference of AR precipitation ratio from its JJA climatology, we find that the ratio increases in the regions where AR precipitation increase while it decreases in the regions where AR precipitation decrease (Figure 5e,f). One exception is the Japanese main islands in which the AR precipitation does not change much, but its ratio significantly

increases and decrease in positive and negative PJ, respectively. This implies that the PJ pattern alters the relative importance of ARs in regional hydroclimate.

3.2. Modulation of hazardous versus beneficial AR events

Not all ARs bring hydrological extremes. Their impacts can be either beneficial or hazardous. The hydrological impacts of ARs are detailed by comparing AR scale which was proposed by Ralph et al. (2019). The AR scale has five ranks, i.e., Cat1–Cat5 (from weak to strong), with differing maximum IVT and duration of AR events at a given location (see the right diagram in Figure 6). The hazardous AR impacts are generally associated with the stronger and locally more persistent AR events (e.g., Cat5 ARs). Although this scaling was originally designed to target landfalling ARs in the U.S. west coast, it has been also applied to western Europe (Eiras–Barca et al., 2021) and even the global domain (Guan et al., 2023). In East Asia summer, higher–rank AR events are more concentrated along the WNPSH boundary (Figure 7). However, we particularly pay

attention to Korea–Japan and eastern China (boxed regions in Figures 3e,f) where the AR activity greatly responds to PJ patterns (see section 3.1). Here, an AR event is defined at each grid point as consecutive time steps during which an AR is observed. Following Park et al. (2023), the 6-h break is allowed in counting AR events to consider the “flickering” issue in the gridded AR data.

In Korea–Japan, the fraction of high–rank AR events is larger in the positive PJ than the one in the negative PJ. The fraction of Cat5 events is particularly increases compared to its climatology. In the negative PJ, the fraction of low–rank AR events is larger than positive PJ. The difference between the positive and negative phases is related to local duration and maximum IVT of AR events (Figure 6c). During the positive PJ, both maximum IVT and local duration increased relative to their climatology, whereas during the negative PJ, both decreased. The magnitude of the increase and decrease is greater in negative PJ, resulting in the greater change in the AR scale.

Conversely, the AR events in eastern China are more hazardous in the negative than positive PJ (Figure 6b). Note

that the fraction of Cat2–Cat5 events in the negative PJ is slightly larger than its climatology. In particular, the fraction of Cat4 events is significantly increased compared to its climatology, with slightly increased local duration of AR events. During the positive PJ, although there is no significant change in AR scale, the fraction of no–rank AR events increases as the local duration of AR events decreases (Figure 6d). However, the inter–phase difference in AR scales is smaller than the one in Korea–Japan (cf. Figures 6a,b), which is likely due to local duration and maximum IVT of AR events increase and decrease in opposite directions.

To sum up, ARs in Korea–Japan become more hazardous in the positive than negative PJ. Likewise, ARs in eastern China pose a greater risk of hydrological extremes in the negative than positive PJ. Combined with section 3.1, the PJ pattern modulates the AR frequency but also the hydrological benefits/hazards of individual ARs, with the latter being closely associated with AR duration.

3.3. Multiscale diagnosis of PJ modulation of ARs

Although the AR response to the PJ pattern is well synchronized with the related WNPSH variability (see Figure 3), it does not explain the detailed mechanisms. The ARs are multiscale in nature, especially in East Asia summer (Park et al., 2023). Indeed, the ARs in East Asia summer are associated with both HF and LF moisture transports which are both pronounced along the WNPSH boundary (Figure 8). This implies that the PJ pattern can modulate the AR activity via not only the intensification/weakening of quasi-stationary monsoon flow (i.e., direct effect) but also the modulation of traveling weather systems (i.e., indirect effect) along the WNPSH boundary. Their relative contribution is assessed in this section by using MI (see Eq. 3).

Figures 9a,b show the PDF of ARs as a function of MI in Korea–Japan, and eastern China, respectively. In Korea–Japan, during the positive PJ, the peak value is about 31% in the MI range of 0.5–0.6. Compared to JJA, the values below 0.6 increase and those above 0.6 decrease. This indicates a

decrease in the contribution of HF processes and an increase in the contribution of LF processes (Figure 9c), resulting in a decrease in the MI value. This indicates an increased contribution of LF processes, which explains the increase in AR duration and hence the increased risk of AR. On the other hand, during negative PJ, the MI distribution is slightly skewed to the right, indicating that the contribution of LF processes has decreased, resulting in the increased value of MI (Figure 9c). The relative decrease in the LF contribution reduces the AR duration and therefore the AR hazard.

In eastern China, during negative PJ, the MI distribution is skewed to the left, indicating the increase in LF contribution, hence the increase in duration. During positive PJ, except for 0.2–0.3, the MI value below 0.6 decreased, with the notable increase of the MI value between 0.7–0.8. This results in an increase in the average MI value (Figure 9d) and hence a decrease in duration.

3.4. Related weather systems

The above results confirm that the relative change in the contribution of $IVTA_{LF}$ leads to the change in AR duration. This section describes the weather conditions that drive the change in $IVTA_{HF}$ and $IVTA_{LF}$. Figure 10 shows the AR–relative composite of the GPH anomaly at 850 hPa and IVTA, and their high–frequency and low–frequency components. The AR–relative composite is constructed with respect to the AR centroid, where the AR centroid is defined by considering the mass–weighted IVT over the grid points covered by the AR.

In Korea–Japan, the negative and positive GPH anomaly are oriented northwest–southeast during the JJA. In between, the positive IVTA develops along the enhanced pressure gradient (Figure 10a). Decomposing the anomalies into high–frequency and low–frequency components shows that both play an important role in shaping the ARs. The high–frequency components show the zonal wave pattern that is part of the transient surface cyclone and anticyclone. A positive $IVTA_{HF}$ appears in the southeastern part of a transient surface cyclone

(Figure 10b). The low-frequency components show the quasi-stationary low and high anomalies, between which a positive $IVTA_{LF}$ develops (Figure 10c). During the positive PJ, positive IVTA appears between two cyclonic and anticyclonic circulations (Figure 10d). The high-frequency component shows moisture transport associated with the surface transient cyclone, which is slightly weakened compared to JJA (Figure 10e). The low-frequency component shows the circulation corresponding to the positive PJ pattern, which is distinct from the average JJA pattern (Figure 10f). This is a result of the PJ pattern directly triggering the circulation. The $IVTA_{LF}$ develops between the circulation directly induced by the PJ pattern and continuously follows the edge of the quasi-stationary anticyclonic circulation. The decreased MI value indicates that the contribution of moisture transport caused by transient cyclones decreases and the moisture supply directly induced by the PJ pattern increases compared to the JJA pattern.

In eastern China, positive IVTA is also found between the negative and positive GPH anomaly during the JJA (Figure 10g). While the magnitude of the two circulations in Korea-

Japan is quite comparable, in eastern China the positive GPH anomaly is well developed relative to the negative GPH anomaly. The high-frequency components reveal the weakened surface transient cyclone compared to the Korea–Japan (Figure 10h). This is consistent with a previous study showing that extratropical cyclone intensity is stronger in Korea–Japan and in the Pacific open ocean (Lee et al., 2019). In the low-frequency component, a positive IVT_{ALF} appears between a weak negative GPH anomaly and a relatively well-developed positive GPH anomaly (Figure 10i). During negative PJ, the high-frequency component also shows moisture transport by a transient cyclone (Figure 10k). In the low-frequency component, a GPH anomaly pattern corresponding to the negative PJ pattern appears, and a positive IVT_{ALF} appears between the two circulations (Figure 10l).

The AR–relative composite for the phase when AR is less frequent in each region is shown in Figure 11. The negative PJ over Korea–Japan shows a surface transient cyclone pattern and a quasi-stationary circulation related to the PJ pattern, while the positive PJ over eastern China does not.

During the positive PJ, the cyclonic circulation centered over Taiwan interrupts the moisture transport from the tropics to eastern China. In other words, the positive PJ pattern does not provide favorable conditions for the occurrence of AR in eastern China, and therefore AR-related synoptic patterns are not well represented during the positive PJ. In summary, $IVTA_{HF}$ appears with a surface transient cyclone, $IVTA_{LF}$ appears with the quasi-stationary circulation directly induced by PJ pattern. This implies that the PJ pattern affects the WNPSH and subsequently the East Asian summer ARs, either by touching an embedded system such as a surface transient cyclone, or by directly altering the quasi-stationary circulation. The change in the relative contribution of the two weather systems to moisture transport results in a change in MI values.

4. Summary and discussion

This study examines the modulation of the PJ pattern on East Asian summertime ARs. During the positive phase of the PJ, the WNPSH expands northwestward, resulting in pronounced AR activity offshore region of South China, the Korean Peninsula, and eastern Japan. In contrast, during the negative phase of the PJ, the WNPSH contracts southward but extends westward. It causes increased AR impacts in eastern China and western Japan. Using the AR categories proposed by Ralph et al. (2019), it is further found that the potential impacts of ARs change. In Korea–Japan, more hazardous ARs increase in positive PJ, and more beneficial ARs increase in negative PJ. This is due to AR duration among the two factors that determine AR category: maximum IVT and AR duration. In eastern China, no significant change in the potential impact of AR is found.

To examine the changes in low–frequency IVTA, which is known to be strongly related to AR duration, IVTA is divided into high–frequency and low–frequency components with a

10-day cut-off time filtering. To examine the relative contribution of each component quantitatively, the MI value, which is the ratio of the high-frequency IVTA to the total IVTA, is used. In Korea-Japan, during the positive PJ, the contribution of low-frequency IVTA increased with MI decreased, and during the negative PJ, the contribution of low-frequency IVTA decreased with MI increased. In eastern China, the changes in MI values for each PJ phase are relatively small. By examining the weather conditions that lead to the difference in each component, an AR-relative composite is constructed with respect to the AR centroid. It reveals that the high-frequency IVTA is associated with the surface transient cyclone, and the low-frequency IVTA is associated with the quasi-stationary circulation directly induced by PJ pattern.

Since ARs are associated with the up to 50% of summer precipitation in East Asia, accurate prediction of ARs on subseasonal to seasonal (S2S) timescales is essential. Several studies have attempted to predict individual ARs, but have been limited by the inability to accurately predict beyond the synoptic weather timescale of 7-10 days (Wick et al., 2013;

Nayak et al., 2014; DeFlorio et al., 2018). In an attempt to improve predictability at S2S timescales, beyond the synoptic weather timescale, DeFlorio et al. (2019) evaluated the prediction skill of ARs at S2S timescales by assessing the AR1wk occurrence, which is the number of AR days per week. Other attempts to improve the forecast skill of ARs include studies that link ARs to slowly varying climate modes. Baggett et al. (2017) suggested that the accuracy of predicting the number of AR strikes per week over Alaska at 14-day lead time improves significantly when both the Madden-Julian oscillation (MJO) phase 7,8 and the easterly quasi-biennial oscillation (QBO) are present. Mundhenk et al. (2018) also showed that the certain MJO and QBO phase combinations provide empirical subseasonal predictive skill for anomalous AR activity. The PJ pattern has been recognized as a possible contributor to S2S predictability (Kosaka et al., 2012, 2013). Consequently, the PJ pattern holds potential for S2S 'forecasts of opportunity', as described in Vitart et al. (2017), where confidence in overall AR activity forecasts increases with consideration of the particular background large-scale climate

variability. Therefore, the link between the PJ pattern and ARs could improve the S2S prediction of ARs and the associated East Asian summer extreme precipitation.

References

- Akbary, M, Salimi, S, Hosseini, S. A., & Hosseini, M. (2019). Spatio-temporal changes of atmospheric rivers in the Middle East and North Africa region. *International Journal of Climatology*.
<https://doi.org/10.1002/joc.60>
- Baggett CF, Barnes E, Maloney E, Mundhenk B. (2017). Advancing atmospheric river forecasts into subseasonal-to-seasonal time scales. *Geophys Res Lett* 44:7528–7536. <https://doi.org/10.1002/2017GL074434>
- Bao, J.-W., Michelson, S. A., Neiman, P. J., Ralph, F. M., & Wilczak, J. M. (2006). Interpretation of enhanced integrated water vapor bands associated with extratropical cyclones: Their formation and connection to tropical moisture. *Monthly Weather Review*, 134, 1063–1080. <https://doi.org/10.1175/mwr3123.1>
- DeFlorio, M. J., Waliser, D. E., Guan, B., Lavers, D. A., Ralph, F. M., & Vitart, F. (2018). Global assessment of atmospheric river prediction skill. *Journal of Hydrometeorology*, 19(2), 409–426.
<https://doi.org/10.1175/JHM-D-17-0135.1>

- DeFlorio, M. J., Waliser, D. E., Guan, B., Ralph, F. M., & Vitart, F. (2019). Global evaluation of atmospheric river subseasonal prediction skill. *Climate Dynamics*, 52(5), 3039–3060. <https://doi.org/10.1007/s00382-018-4309>
- Dettinger MD, Ralph FM, Das T (2011). Atmospheric rivers, floods and the water resources of California (special issue: Managing water resources and development in a changing climate). *Water* 3(2):445–478. <https://doi.org/10.3390/w3020445>
- Dhana Laskhmi, D., & Satyanarayana, A. N. V. (2020). Climatology of landfalling atmospheric Rivers and associated heavy precipitation over the Indian coastal regions. *International Journal of Climatology*, 40. <https://doi.org/10.1002/joc.65>
- Duchon, C. E. (1979). Lanczos filtering in one and two dimensions. *Journal of Applied Meteorology and Climatology*, 18, 1016–1022. [https://doi.org/10.1175/1520-0450\(1979\)018<1016:LFIOAT>2.0.CO;2](https://doi.org/10.1175/1520-0450(1979)018<1016:LFIOAT>2.0.CO;2)
- Eiras-Barca, J., Ramos, A. M., Algarra, I., Vázquez, M., Dominguez, F., Miguez-Macho, G., et al. (2021). European West Coast atmospheric rivers: A scale to characterize strength and impacts.

Weather and Climate Extremes, 31, 100305.
<https://doi.org/10.1016/j.wace.2021.100305>

Gimeno, L., Algarra, I., Eiras-Barca, J., Ramos, A. M., & Nieto, R. (2021). Atmospheric river, a term encompassing different meteorological patterns. *WIREs Water*, 8(6), e1558. <https://doi.org/10.1002/wat2.1558>

Guan, B., and Waliser, D. E. (2015) Detection of atmospheric rivers: evaluation and application of an algorithm for global studies. *Journal of Geophysical Research–Atmosphere*, 120, 12514–12535. <https://doi.org/10.1002/2015JD024257>

Guan, B., Waliser, D. E., & Ralph, F. M. (2023). Global application of the atmospheric river scale. *Journal of Geophysical Research: Atmospheres*, 128, e2022JD037180. <https://doi.org/10.1029/2022JD037180>

Hersbach, H., Bell, B., Berrisford, P., Hirahara, S., Horányi, A., Muñoz-Sabater, J., et al. (2020). The ERA5 global reanalysis. *Quarterly Journal of the Royal Meteorological Society*, 146, 1999–2049. <https://doi.org/10.1002/qj.3803>

Kamae, Y., Mei, W., Xie, S.-P., Naoi, M., and Ueda, H. (2017a).

Atmospheric rivers over the Northwestern Pacific: Climatology and interannual variability. *Journal of Climate*, 30, 5605–5619. <https://doi.org/10.1175/JCLI-D-16-0875.1>

Kamae, Y., Mei, W., and Xie, S.-P. (2017b). Climatological relationship between warm season atmospheric rivers and heavy rainfall over East Asia. *Journal of the Meteorological Society of Japan* Series II, 95, 411–431. <https://doi.org/10.2151/jmsj.2017-027>

Kim, J., Moon, H., Guan, B., Waliser, D. E., Choi, J., Gu, T. Y., and Byun, Y. H. (2021). Precipitation characteristics related to atmospheric rivers in East Asia. *International Journal of Climatology*, 41, E2244–E2257. <https://doi.org/10.1002/joc.6843>

Kosaka, Y., & Nakamura, H. (2006). Structure and dynamics of the summertime Pacific–Japan teleconnection pattern. *Quarterly Journal of the Royal Meteorological Society*, 132(619), 2009–2030. <https://doi.org/10.1256/qj.05.204>

Kosaka, Y., Xie, S.-P., & Nakamura, H. (2011). Dynamics of interannual variability in summer precipitation over East Asia. *Journal of Climate*, 24(20), 5435–5453.

<https://doi.org/10.1175/2011JCL>

Kosaka, Y., Chowdary, J. S., Xie, S. P., Min, Y. M., & Lee, J. Y. (2012). Limitations of seasonal predictability for summer climate over East Asia and the Northwestern Pacific. *Journal of Climate*, 25(21), 7574–7589. <https://doi.org/10.1175/JCLI-D-12-00009.1>

Kosaka, Y., Xie, S. P., Lau, N. C., & Vecchi, G. A. (2013). Origin of seasonal predictability for summer climate over the Northwestern Pacific. *Proceedings of the National Academy of Sciences of the United States of America*, 110(19), 7574–7579. <https://doi.org/10.1073/pnas.1215582110>

Kubota, H., Kosaka, Y., & Xie, S. (2016). A 117-year long index of the Pacific–Japan pattern with application to interdecadal variability. *International Journal of Climatology*, 36(4), 1575–1589. <https://doi.org/10.1002/joc.4441>

Kwon, Y., Park, C., Back, S.–Y., Son, S.–W., Kim, J., Cha, E.J. (2022). Influence of atmospheric rivers on regional precipitation in South Korea. *Atmosphere* 32, 135–148. <https://doi.org/10.14191/Atmos.2022.32.2.135>

- Lee J, Son S–W, Cho H–O, Kim J, Cha D–H, Gyakum J R and Chen D. (2019). Extratropical cyclones over East Asia: climatology, seasonal cycle, and long–term trend. *Clim. Dyn.* 54 1131–44. <https://doi.org/10.1007/s00382-019-05048-w>
- Liang, J., & Yong, Y. (2021). Climatology of atmospheric rivers in the Asian monsoon region. *International Journal of Climatology*, 41, E810–E818. <https://doi.org/10.1002/joc.6729>
- Mundhenk, B., Barnes, E. A., Maloney, E. D. (2016). All–season climatology and variability of atmospheric rivers over the North Pacific. *Journal of Climate*, 29, 4885–4903. <https://doi.org/10.1175/JCLI-D-15-0655.1>.
- Mundhenk B, Barnes E, Maloney E, Baggett C. (2018). Skillful empirical subseasonal prediction of landfalling atmospheric river activity using the Madden–Julian oscillation and quasi–biennial oscillation. *NPJ Clim Atmos Sci* 1:7. <https://doi.org/10.1038/s41612-017-0008-2>
- Naoi, M., Kamae, Y., Ueda, H., & Mei, W. (2020). Impacts of seasonal transitions of ENSO on atmospheric river activity over East Asia. *Journal of the Meteorological Society of Japan*, 98, 655–668.

<https://doi.org/10.2151/jmsj.2020-027>

Nash, D., Waliser, D., Guan, B., Ye, H., & Ralph, F. M. (2018). The role of atmospheric rivers in extratropical and polar hydroclimate. *Journal of Geophysical Research: Atmospheres*, 123(13), 6804–6821. <https://doi.org/10.1029/2017jd028130>

Nayak MA, Villarini G, Lavers D. (2014). On the skill of numerical weather prediction models to forecast atmospheric rivers over the central United States. *Geophys Res Lett* 41:4354–4362. <https://doi.org/10.1002/2014GL060299>

Nayak, M. A., & Villarini, G. (2017). A long-term perspective of the hydroclimatological impacts of atmospheric rivers over the central United States. *Water Resources Research*, 53(2), 1144–1166. <https://doi.org/10.1002/2016WR019033>

Neiman, P. J., Ralph, F. M., Wick, G. A., Lundquist, J. D., & Dettinger, M. D. (2008). Meteorological characteristics and overland precipitation impacts of atmospheric rivers affecting the West coast of North America based on eight years of SSM/I satellite observations. *Journal of Hydrometeorology*, 9, 22–47. <https://doi.org/10.1175/2007JHM855.1>

- Nitta, T. (1987). Convective activities in the Tropical Western Pacific and their impact on the Northern Hemisphere Summer Circulation. *Journal of the Meteorological Society of Japan*. Series II, 65(3), 373–390. https://doi.org/10.2151/jmsj1965.65.3_373
- Noh, E. et al. (2021). The role of the pacific–japan pattern in extreme heatwaves over Korea and Japan. *Geophysical Research Letters*, 48, 1–12. <https://doi.org/10.1029/2021GL093990>
- Paltan, H., Waliser, D., Lim, W. H., Guan, B., Yamazaki, D., Pant, R., Dadson, S. (2017). Global floods and water availability driven by atmospheric rivers. *Geophysical Research Letters*, 44, 10387–10395. <https://doi.org/10.1002/2017GL074882>.
- Pan, M., & Lu, M. (2020). East Asia atmospheric river catalog: Annual cycle, transition mechanism, and precipitation. *Geophysical Research Letters*, 47, e2020GL089477. <https://doi.org/10.1029/2020GL089477>
- Park, C., Son, S.–W., and Kim, H. (2021). Distinct features of atmospheric rivers in the early versus late east Asian summer monsoon and their impacts on monsoon rainfall. *Journal of Geophysical Research: Atmosphere*, 126, e2020JD033537.

<https://doi.org/10.1029/2020JD033537>

Park, C., Son, S.-W., & Guan, B. (2023). Multiscale nature of atmospheric rivers. *Geophysical Research Letters*, 50, e2023GL102784. <https://doi.org/10.1029/2023GL1027>

Ralph, F. M., Neiman, P. J., Wick, G. A., Gutman, S. I., Dettinger, M. D., Cayan, D. R., and White, A. B. (2006). Flooding on California's Russian River: Role of atmospheric rivers. *Geophysical Research Letters*, 33, L13801, <https://doi.org/10.1029/2006GL026689>

Ralph FM, Dettinger MD (2012). Historical and national perspectives on extreme west-coast precipitation associated with atmospheric rivers during December 2010. *Bull Am Meteor Soc* 93(6):783–790. <https://doi.org/10.1175/BAMS0D-11-001881>

Ralph, F. M., Rutz, J. J., Cordeira, J. M., Dettinger, M., Anderson, M., Reynolds, D., Schick, L. J., & Smallcomb, C. (2019). A scale to characterize the strength and impacts of atmospheric rivers. *Bulletin of the American Meteorological Society*, 269–289, <https://doi.org/10.1175/BAMS-D-18-0023>

Viale, M., Valenzuela, R., Garreaud, R. D., and Ralph, F. M. (2018). Impacts of atmospheric rivers on precipitation in southern South

America. *Journal of Hydrometeorology*, 19, 1671–1687.
<https://doi.org/10.1175/JHM-D-18-0006.1>.

Vitart F et al (2017). The subseasonal to seasonal (S2S) prediction project database. *Bull Am Meteor Soc* 98(1):163–176.
<https://doi.org/10.1175/BAMS-D-16-0017.1>

Waliser, D., and Guan, B. (2017). Extreme winds and precipitation during landfall of atmospheric rivers. *Nature Geoscience*, 10, 179–183. <https://doi.org/10.1038/NGEO2894>

Wick GA, Neiman P, Ralph F, Hamill T. (2013). Evaluation of forecasts of the water vapor signature of atmospheric rivers in operational numerical weather prediction models. *Weather Forecast*, 28(6):1337–1352. <https://doi.org/10.1175/WAF-D-13-00025.1>

Wille, J. D., Favier, V., Dufour, A., Gorodetckaya, I. V., Turner, J., Agosta, C., & Codron, F. (2019). West Antarctic surface melt triggered by atmospheric rivers. *Nature Geoscience*, 12, 911–916, <https://doi.org/10.1038/s41561-019-0460-1>

Xie, S.-P., Hu, K., Hafner, J., Tokinaga, H., Du, Y., Huang, G., & Sampe, T. (2009). Indian Ocean capacitor effect on Indo-

Western Pacific climate during the summer following El Niño.
Journal of Climate, 22(3), 730–747.
<https://doi.org/10.1175/2008JCLI2544.1>

Xie, S.-P., Kosaka, Y., Du, Y., Hu, K., Chowdary, J. S., & Huang, G. (2016). Indo-western Pacific ocean capacitor and coherent climate anomalies in post-ENSO summer: A review. *Advances in Atmospheric Sciences*, 33, 411–432.
<https://doi.org/10.1007/s00376-015-5192-6>

Xie, P., Yatagai, A., Chen, M., Hayasaka, T., Fukushima, Y., Liu, C., & Yang, S. (2007). A gauge-based analysis of daily precipitation over east Asia. *Journal of Hydrometeorology*, 8, 607–626.
<https://doi.org/10.1175/JHM583.1>

Ye, C., Zhang, H., Moise, A., & Mo, R. (2020). Atmospheric rivers in the Australia–Asian region: a BoM–CMA collaborative study. *Journal of Southern Hemisphere Earth Systems Science*, 70, 3–16. <https://doi.org/10.1071/ES19025>

Figures

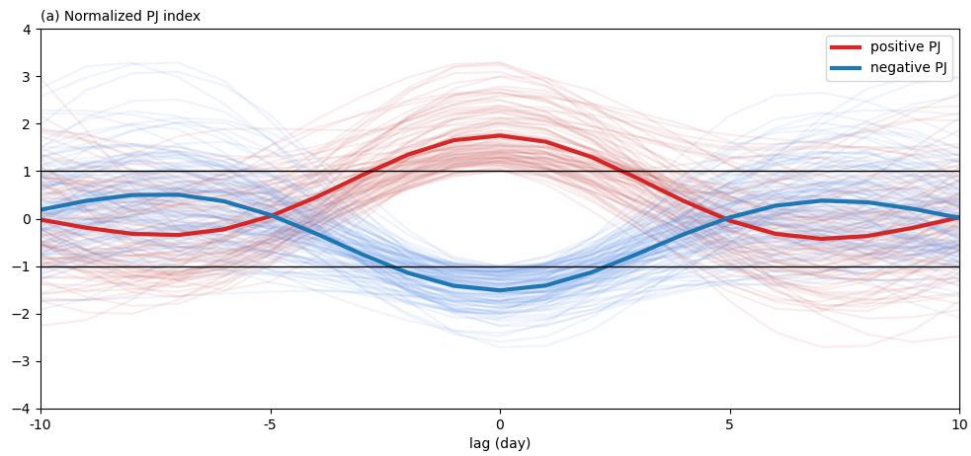


Figure 1. The normalized time series distribution of the PJ index during positive PJ (red line), and negative PJ (blue line). The thin lines indicate individual PJ event indices, while the thick lines are the average. The black lines denote the ± 1 standard deviation of the PJ index.

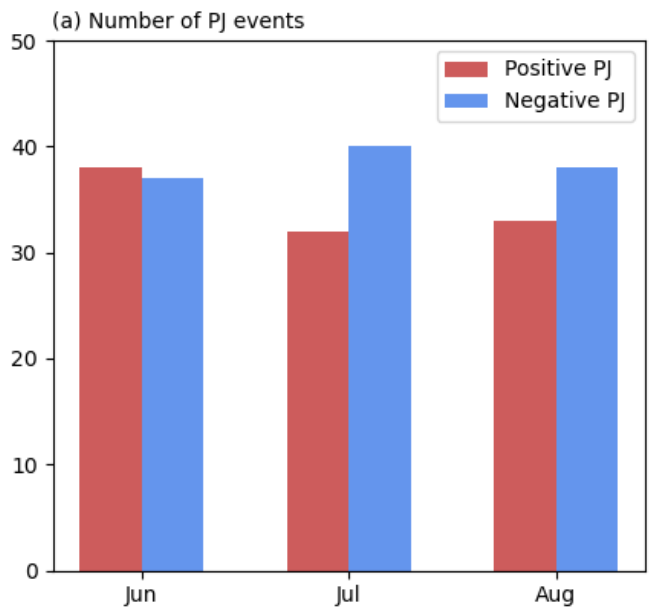


Figure 2. The number of positive PJ events (red bars), and negative PJ events (blue bars) in June, July, and August from 1979 to 2020.

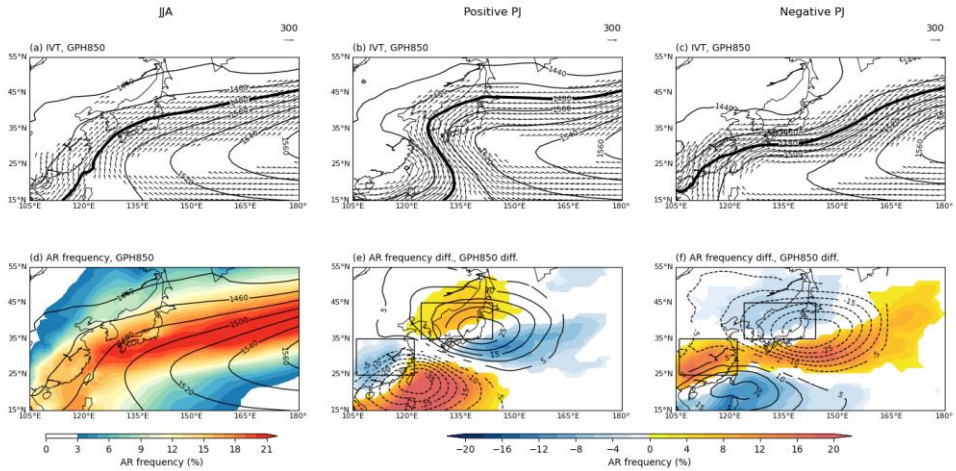


Figure 3. (a) JJA climatology of **IVT** ($> 150 \text{ kg m}^{-1} \text{ s}^{-1}$, vectors), and 850-hPa GPH (gpm, contoured). (b), (c) As in (a) but for (b) positive PJ, and (c) negative PJ. (d) JJA climatology of AR frequency (%), shaded), and 850-hPa GPH (gpm, contoured). (e), (f) Differences of AR frequency (%), shaded), and 850-hPa GPH (gpm, contoured) from JJA climatologies for (e) positive PJ, and (f) negative PJ. Only the statistically significant differences are shown based on two-tailed student's *t* test at the 95% confidence level. The number of degrees of freedom corresponds to the number of PJ events. In (a) – (f), the WNPSH boundary is highlighted by a bold 1,480-gpm contour. The black boxed regions in (e), (f) denote the Korea–Japan ($35\text{--}45^\circ \text{ N}$, $124\text{--}144^\circ \text{ E}$) and eastern China ($25\text{--}35^\circ \text{ N}$, $106\text{--}122^\circ \text{ E}$) domains in this study.

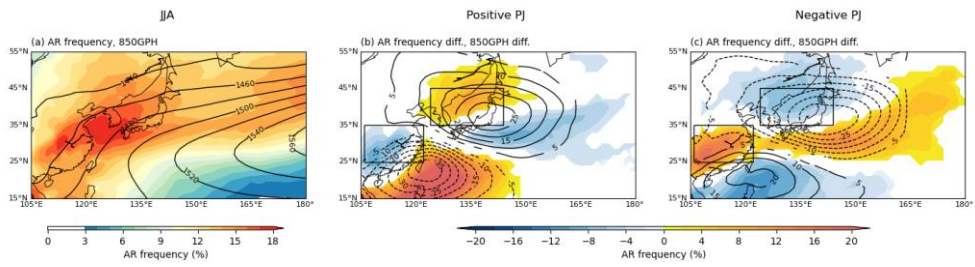


Figure 4. As in Fig. 3d–f, but derived from the original Guan and Waliser (2015) algorithms.

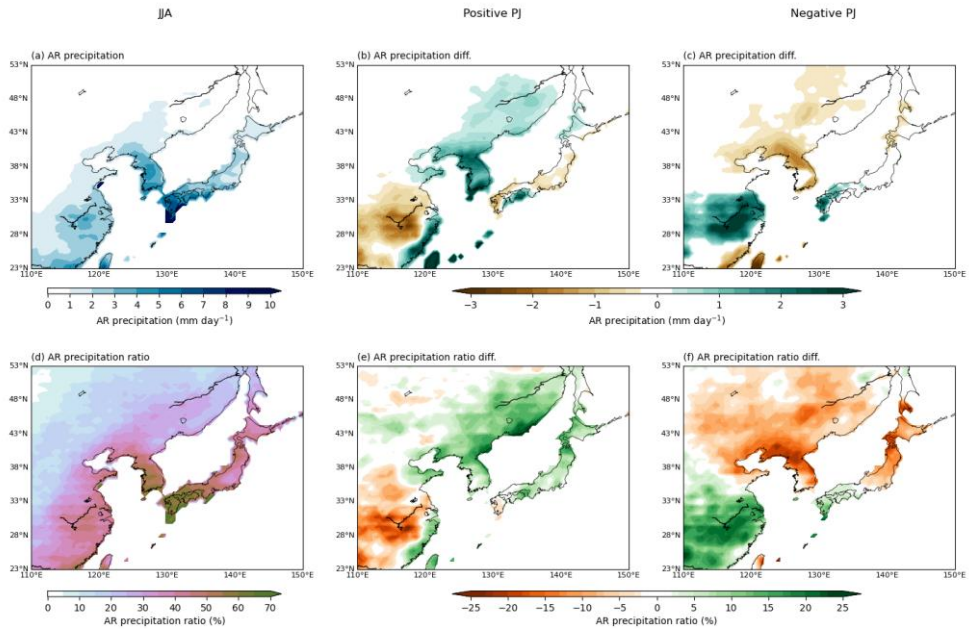


Figure 5. (a) JJA climatology of AR precipitation (mm day^{-1} , shaded). (b), (c) Differences in AR precipitation (mm day^{-1} , shaded) from JJA climatologies for (b) positive PJ, and (c) negative PJ. Only the statistically significant difference is displayed based on two-tailed student's t test at the 95% confidence level. The number of degrees of freedom corresponds to the number of independent PJ events. (d) – (f) As in (a) – (c), but for AR precipitation ratio (% , shaded).

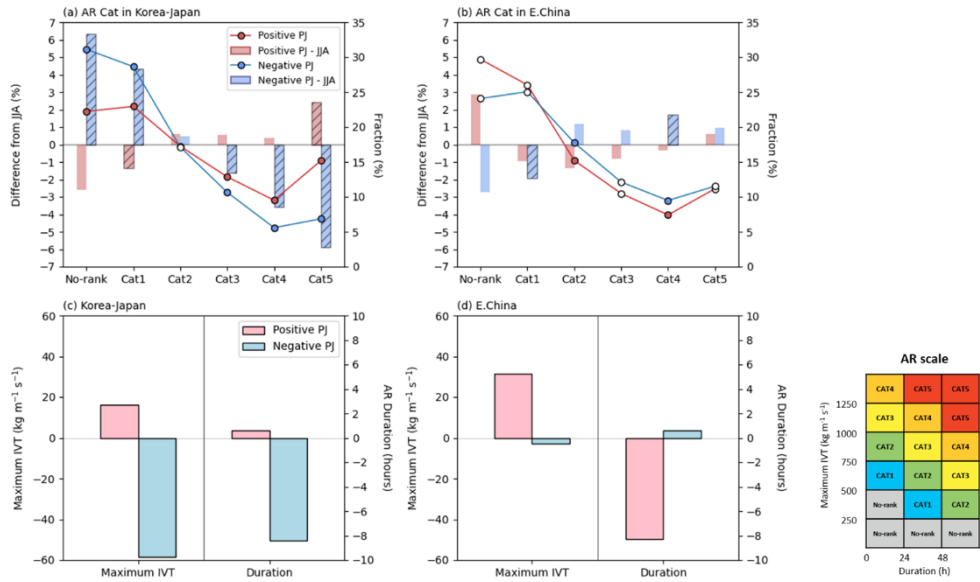


Figure 6. (a),(b) Fraction of AR events for five different AR scales (see the right diagram) during positive PJ (red line), and negative PJ (blue line) in (a) Korea–Japan, and (b) eastern China. Filled circles indicate statistically significant differences between the two PJ phases based on two–tailed student’ s t test at the 95% confidence level. Red and blue bars represent the difference in fraction (%) from JJA climatology for positive PJ, and negative PJ, respectively. Hatched bars indicate statistically significant differences between the JJA and each PJ phase based on two–tailed student’ s t test at the 95% confidence level. (c),(d) Differences in maximum IVT (left y–axis), and AR duration (right y–axis) for AR events from JJA climatologies in the (c) Korea–Japan, and (d) eastern China for positive PJ (red box), and negative PJ (blue box). The ARs whose

centroids are located in the boxed regions in Figs. 3e,f are considered.

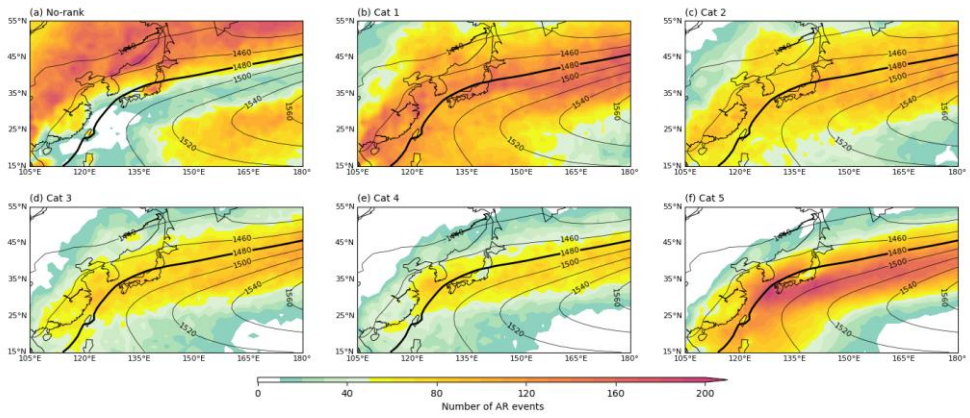


Figure 7. The number of AR events during 1979–2020 JJA depending on AR scales (shaded) overlaid with 850–hPa GPH climatology (gpm, contoured). The WNPSH boundary is highlighted by a bold 1,480–gpm contour.

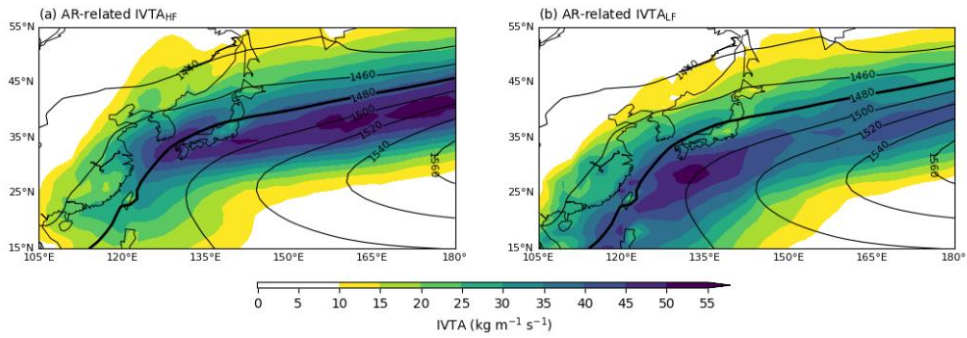


Figure 8. JJA climatology of (a) AR-related IVTA_{HF} ($\text{kg m}^{-1} \text{s}^{-1}$, shaded), and (b) AR-related IVTA_{LF} ($\text{kg m}^{-1} \text{s}^{-1}$, shaded) overlaid with 850-hPa GPH (gpm, contoured). The AR-related IVTA components are determined by considering the spatial overlap of AR and IVTA.

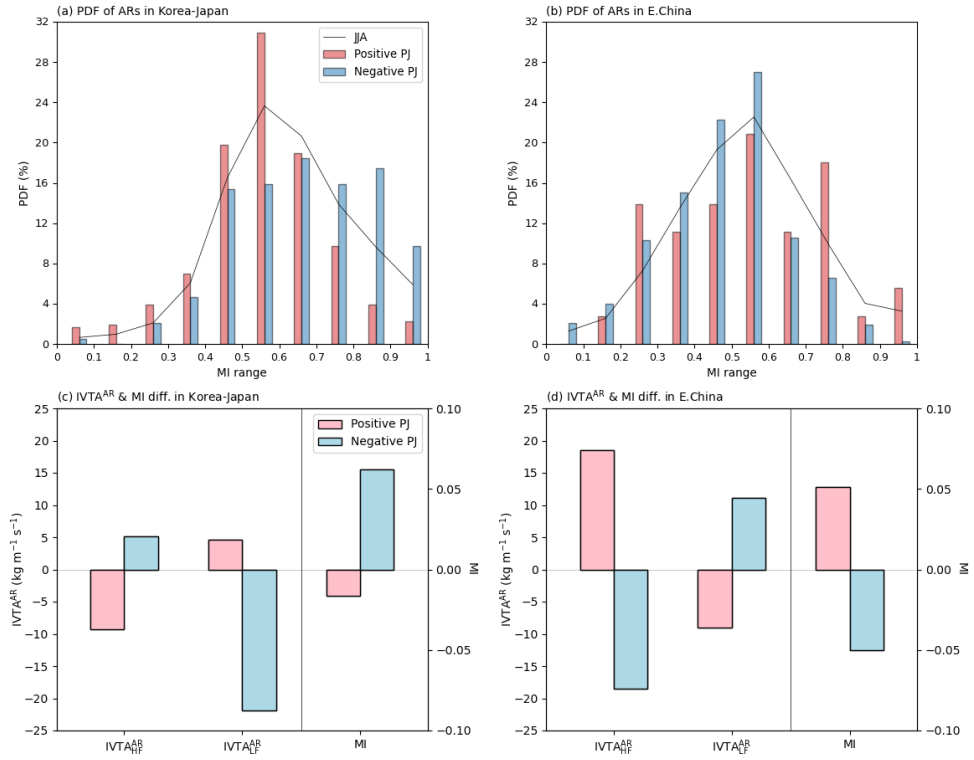


Figure 9. (a),(b) PDF (%) of ARs in (a) Korea–Japan, and (b) eastern China as a function of MI during JJA (black line), positive PJ (red bars), and negative PJ (blue bars). (c),(d) Differences in $IVTA_{HF}^{AR}$ (left y-axis), $IVTA_{LF}^{AR}$ (left y-axis), and MI (right y-axis) from JJA climatologies in the (c) Korea–Japan, and (d) eastern China for positive PJ (red box), and negative PJ (blue box). The ARs whose centroids are located in the boxed regions in Figs. 3e,f are considered.

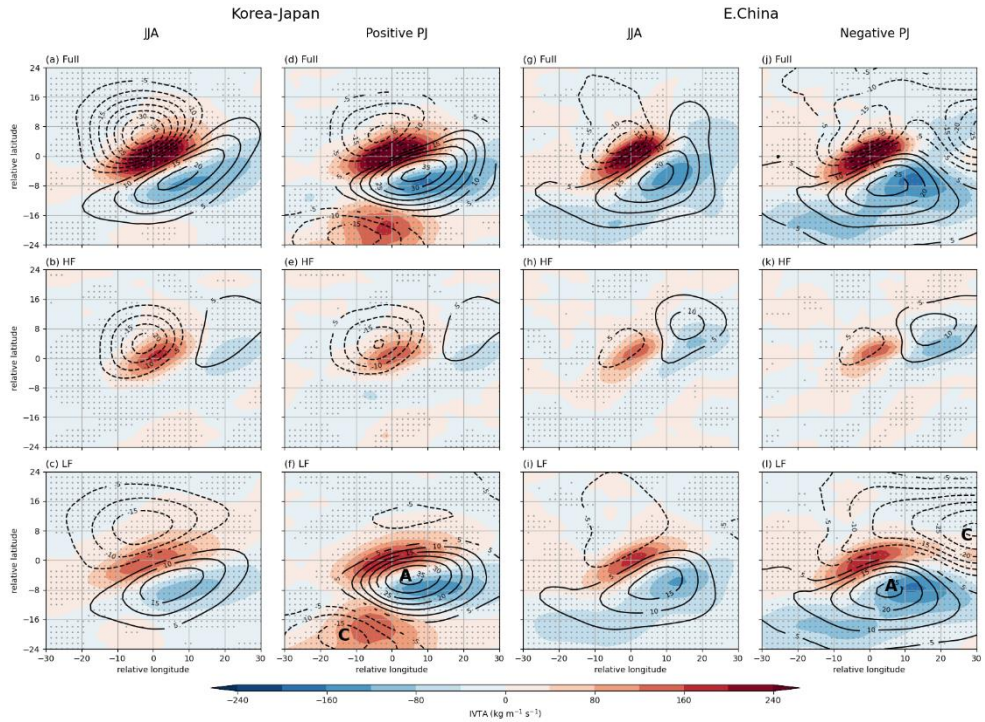


Figure 10. (a) – (f) AR–relative composites of (top) 850–hPa GPHA (gpm, contoured) and IVTA ($\text{kg m}^{-1} \text{s}^{-1}$, shaded), and their (middle) HF and (lower) LF components during (a) – (c) JJA, (d) – (f) positive PJ for ARs in Korea–Japan. Only the statistically significant GPHA is shown based on two–tailed student’ s t test at the 95% confidence level. Stipples indicate the statistically significant IVTA. The number of degrees of freedom is determined by regarding consecutive six–hourly AR snapshots as one event. (g) – (i) As in (a) – (c), but for ARs in eastern China. (j) – (l) As in (d) – (f), but for ARs in eastern China during negative PJ. In (f),(l), “A” and “C” indicate the PJ–related LF anticyclone and cyclone, respectively. The ARs whose

centroids are located in the boxed regions in Figs. 3e,f are considered.

국문 초록

Pacific-Japan 패턴에 의한 동아시아 atmospheric river 의 조절

권 예 은
지구환경과학부
석사과정
서울대학교

Atmospheric river (AR) 는 강하고 좁게 발생하는 수증기 수송 현상으로 동아시아 국가에 큰 수문학적 영향을 끼친다. 최근 연구들을 통해 동아시아 AR의 기후학적 특성이 잘 알려졌으나, 계절 내 변동성에 대해서는 아직 밝혀진 바가 많지 않다. 본 연구는 여름철 동아시아 AR의 계절 내 변동성을 Pacific-Japan (PJ) 패턴과 연관 지어 설명하고자 한다. 동아시아 여름철 AR은 PJ 패턴에 의해 뚜렷한 변화를 보인다. PJ 패턴이 양의 패턴일 때, 북서태평양 고기압이 북서쪽으로 확장하며 한국과 일본에서 AR의 활동성이 강화된다. 반대로 음의 패턴일 때, 북서태평양 고기압이 남쪽으로 후퇴하며 서쪽으로 길게 늘어지는데 이는 동중국에서의 AR 활동성을 강화 시킨다. AR 활동성이 강화되는 패턴(즉, 한국과 일본에서의 양의 패턴, 동중국에서의 음의 패턴) 일 때 AR의 지속시간도 증가하게 되는데 이는 더 위험한 AR이 증가함을 의미한다. 이러한 변화는 PJ 패턴에 의해 직접적으로 유도되는 준정체적인(quasi-stationary) 수증기 수송과 날씨 시스템이 간접적인 영향을 받아 변하는 일시적인(transient) 수증기 수송에 의해 발생한다. 본 연구는 PJ 패턴을 모니터링 함으로써 동아시아 AR의 이해 및 예측성 향상에 도움이 될 수 있음을 시사한다.

주요어: atmospheric river, Pacific–Japan 패턴, 계절 내 변화

학번: 2021-26855